Title

Enhancement of thermoelectric properties in the Nbâ��Coâ��Sn half-Heusler/Heusler system through spontaneous inclusion of a coherent second phase

Journal

Journal of Applied Physics, 120(7)

ISSN

0021-8979 1089-7550

Authors

Buffon, Malinda L. C
Laurita, Geneva
Verma, Nisha
et al.

Publication Date

2016-08-21

DOI

10.1063/1.4961215

Peer reviewed

Enhancement of Thermoelectric Properties in the Nb–Co–Sn Half-Heusler/Heusler System Through Spontaneous Inclusion of a Coherent Second Phase

Malinda L. C. Buffon,[1,2,a)] Geneva Laurita,[2] Nisha Verma,[1,2] Leo Lamontagne,[1,2] Leila Ghadbeigi,[3] Demetrious L. Lloyd,[2,4] Taylor D. Sparks,[3] Tresa M. Pollock,[1,2] and Ram Seshadri[1,2,4]

[1)] *Materials Department, University of California, Santa Barbara, CA 93106*

[2)] *Materials Research Laboratory, University of California, Santa Barbara, CA 93106*

[3)] *Materials Science and Engineering, University of Utah, UT 84112*

[4)] *Department of Chemistry and Biochemistry, University of California, Santa Barbara, CA 93106*

(Dated: 7 July 2016)

Half-Heusler XYZ compounds with an 18 valence electron count are promising thermoelectric materials, being thermally and chemically stable, deriving from relatively earth-abundant components, and possessing appropriate electrical transport properties. The typical drawback with this family of compounds is their high thermal conductivity. A strategy for reducing thermal conductivity is through the inclusion of secondary phases designed to minimize negative impact on other properties. Here, we achieve this through the addition of excess Co to half-Heusler NbCoSn, which introduces precipitates of a semi-coherent $NbCo_2Sn$ Heusler phase. A series of $NbCo_{1+x}Sn$ materials are characterized here using X-ray and neutron diffraction studies and electron microscopy. Electrical and thermal transport measurements and electronic structure calculations are used to understand property evolution. We find that annealing has an important role to play in determining antisite ordering and properties. Antisite disorder in the as-prepared samples improves thermoelectric performance through the reduction of thermal conductivity, but annealing during the measurement degrades properties to resemble those of the annealed samples. Similar to the more widely studied $TiNi_{1+x}Sn$ system, Co addition to the NbCoSn phase results in improved thermoelectric performance through a decrease in thermal conductivity which results in a 20% improvement in the thermoelectric figure of merit, zT.

INTRODUCTION

Due to their unique ability to convert a temperature gradient into a voltage differential, thermoelectric materials provide a pathway towards the sustainable harvest of waste heat. The performance of a thermoelectric material is captured by the dimensionless thermoelectric figure of merit, $zT = [S^2/(\kappa\rho)]T$, where at temperature T, S is the Seebeck coefficient, κ is the total thermal conductivity, and ρ is the electrical resistivity of a material.[1] Various material classes such as main group chalcogenides,[2] silicides,[3] Si–Ge alloys,[4] clathrates,[5] skutterudites,[6] oxides,[7] Zintls,[8] and half-Heusler compounds[9] have been explored and optimized for zT.

Half-Heusler compounds, in particular, feature large Seebeck coefficients ($|S| > 200\,\mu$V/K) with appropriate low electrical resitivities, and can be prepared from relatively earth-abundant and available materials, making them attractive candidates for thermoelectric applications.[10] Heusler compounds were first synthesized in 1903 by Heusler who discovered that, despite containing no magnetic elements, $MnCu_2Al$ exhibited ferromagnetic behavior.[11] This led to the discovery of multiple large structural classes of materials, including half-Heusler (hH) and Heusler (H) compounds. Compounds with these structures have unique properties that result in a broad range of applications including magnetic tunnel junctions,[12] topological insulators,[13] superconductivity,[14] magnetocalorics,[15] and thermoelectrics.[10]

The half-Heusler (hH) and Heusler (H) crystal structures are shown in Figure 1, and are described in detailed in the caption. hH compounds have the chemical formula XYZ, while the H compounds have the formula $XYY'Z$, or XY_2Z, where X and Y are typically transition metals and Z is a main group element. As X and Z usually have the largest electronegativity difference, these elements form a rock-salt structure with the Y atoms filling the tetrahedral voids of the rocksalt lattice.[16] The hH crystal structure can be described as a zinc blende sublattice, formed by Y and Z atoms, where half of tetrahedral vacancies are stuffed by X atoms. Within this perspective, the valence electrons from the electropositive X^{n+} are transferred to the more electronegative $(YZ)^{n-}$. When the total valence electron count (VEC) is eight or eighteen, the compound has a full shell and is expected to be semiconducting.[17] These semiconducting hH compounds are valuable compounds for thermoelectric applications, displaying the desirable combination of high Seebeck coefficient, coupled with relatively low electrical resistivities. However, they also exhibit high thermal conductivities κ on the order of $\kappa = 10\,\mathrm{W\,m^{-1}\,K^{-1}}$,[10] in contrast to canonical materials, such as the heavy main group chalcogenides, that can possess values of κ that are smaller. Effective methods for lowering κ, thus improving

[a)] Electronic mail: mandibuffon@mrl.ucsb.edu

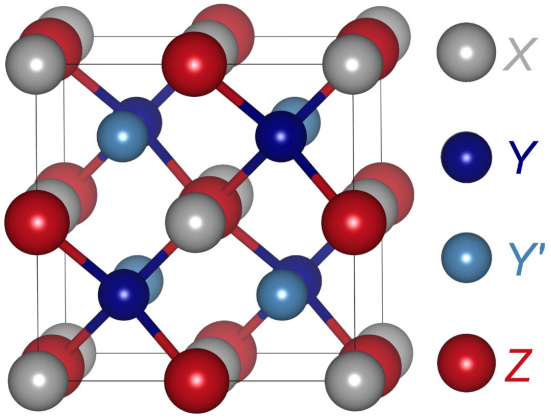

FIG. 1. Depiction of the crystal structures of cubic half-Heusler (hH), XYZ and cubic Heusler (H), $XYY'Z$ compounds described in the face-centered cubic space groups $F\bar{4}3m$ and $Fm\bar{3}m$, respectively. In both structures X are in the $4a$ Wyckoff site $(0,0,0)$, while Z are in $4b$ $(\frac{1}{2},\frac{1}{2},\frac{1}{2})$. In the hH structure, Y atoms are in $4c$ $(\frac{1}{4},\frac{1}{4},\frac{1}{4})$. In the H structure Y and $Y\prime$ (which are the same atom) are in $8c$ $(\frac{1}{4},\frac{1}{4},\frac{1}{4})$ in $Fm\bar{3}m$. The diamondoid tetrahedral network formed by the Y–Z atoms of hH is indicated with bonds.

zT, for this system includes doping,[18] site substitution,[19] and nanostructuring to introduce phonon scattering centers in the material.[20]

A method of choice for lowering κ in hH–derived materials employs the spontaneous phase separation between hH and H phases to form a biphasic material. In this approach, extra Y atoms are added to the starting compositions of XYZ hH, resulting, after suitable processing in a material of a hH matrix with H inclusions that act as phonon scattering centers. Douglas *et al.*[21] have employed this approach for the Ti–Ni–Sn system, forming a continuous hH TiNiSn matrix with discrete H $TiNi_2Sn$ inclusions. Three dimensional microstructural analysis of $TiNi_{1.20}Sn$ suggests the eventual percolation of the H phase at large Ni additions, which degrades zT as compared to $TiNi_{1.15}Sn$.[22] Detailed investigation of this two phase system shows that some excess Ni tends to enter the tetrahedral vacancies of the hH matrix, permitting this phase to exist at off stoichiometric concentrations. Continued additions of Ni results in the formation of small H clusters.[23] Similarly, the addition of Ni in (Zr,Hf)–Ni–Sn systems reveals phase separation to a mixture of H and hH phases,[24] and that that there is a relationship between structural ordering in (Ti,Zr,Hf)–Ni–Sn hH materials and thermoelectric properties[26]. The combined effect of H inclusions and tetrahedral interstitials introduces phonon scattering at a range of length scales, leading to further reduction in κ.[25] Here we explore this approach in an alternate hH–H system: Nb–Co–Sn.

NbCoSn (hH) and $NbCo_2Sn$ (H) compounds are reported to be stable in the Nb–Co–Sn phase space.[27] NbCoSn hH was selected due to its 18 valence electron count. NbCoSn has been explored for thermoelectric applications by Ono *et al.*, who investigated the effect of Sb–doping on the thermoelectric properties,[27] while Kimura *et al.* explored biphasic $NbCo_{1+x}Sn$, $x = 0.00$, 0.05, 0.10, prepared by optical float zone, indicating that it is possible to reduce the thermal conductivity of NbCoSn through the addition of Co.[28,29]

In this work, we will show that the hH phase of NbCoSn can be formed without the annealing step required for most hH materials, including TiNiSn. The absence of annealing for NbCoSn phase formation allows the study of how preparation and subsequent ordering in hH materials impacts observed thermoelectric properties. Here we study the Nb–Co–Sn hH–H system and examine the effect of the second-phase inclusions on the properties, as well as the role played by antisite disorder.

EXPERIMENTAL DETAILS

A series of $NbCo_{1+x}Sn$ ($x = 0.00$, 0.05, 0.10, 0.15, 0.20) samples were prepared, as described in more detailed below. Compositions were selected to be in the biphasic regime between the hH and H phases to maximize thermoelectric properties as illustrated by previous work on the Ti–Ni–Sn system.[21] Samples were characterized through X-ray and neutron powder diffraction, microscopy, and thermoelectric property measurements. Density functional theory (DFT) calculations were performed to examine the electronic band structure for the possible origins of the high Seebeck coefficient, as well as to approximate the value of the minimum thermal conductivity κ_{min} of NbCoSn, following Clarke's treatment.[30]

To determine the effect of annealing on the structural and thermoelectric properties, samples were prepared using two different approaches, indicated as "as-prepared" (AP) and "annealed" (An). The AP samples were first arc-melted in an Ar atmosphere from a stoichiometric ratio of the pure elements: Nb foil (99.8%, Sigma Aldrich), Co powder (99.9%, Sigma Aldrich), and Sn shot (99.8%, Sigma Aldrich). The samples were flipped between each melt, and melted a total of three times to ensure homogeneity. The mass loss during melting was less than 2% for all samples. The An samples were then wrapped in Ta foil, placed in an evacuated fused silica ampoule, and submitted to an additional annealing step at 1123 K for 1 week. Both AP and An samples were subsequently pulverized in a WC ball-mill for 5 min, and powders were then loaded in a 20 mm diameter die for further consolidation by spark plasma sintering (SPS). Samples were pressed in the SPS for 5 minutes at 50 MPa at 1123 K. The resulting samples were approximately 7 g in mass. Electrical discharge machining was used to section samples to appropriate dimensions for measurements.

Room temperature synchrotron X-ray diffraction (XRD) data were acquired for all samples at the Advanced Photon Source at the 11-BM beamline at Argonne National Laboratory. Samples were placed in Kap-

ton capillaries and a wavelength of 0.4592 Å was selected to avoid resonant Sn absorption. Room temperature neutron diffraction data were acquired on the POWGEN diffractometer at Oak Ridge National Laboratory for $x = 0.00$ *AP* and $x = 0.00$, 0.15 *An* samples. Samples were loaded into 6 mm vanadium cans and data was collected for approximately 2 h per sample. Refinement of all diffraction data was completed using the Rietveld method as implemented in the GSAS-EXPGUI suite of programs.[31,32] Sn occupancy was held at 1 while allowing the Co and Nb site occupancies to vary. Crystal structures were visualized using VESTA.[33]

The microstructure of each sample was examined by removing a small piece from the bulk sample, mounting it in epoxy, and polishing with SiC and then with diamond suspension, finishing with 0.25 μm diamond suspension. Scanning electron microscopy (SEM) studies were carried out on a FEI XL30 Sirion FEG microscope equipped with a backscattered-electron (BSE) detector. Energy dispersive X-ray (EDX) analysis assisted in phase identification. TEM lamella were prepared using a focused ion beam (FIB, Helios, FEI). Detailed investigation of microstructure was conducted in Tecnai G2 sphera TEM (FEI) operating at 300 keV.

Electrical transport properties (electrical conductivity and Seebeck coefficient) were measured on 2 mm × 2 mm × 8 mm bars on an ULVAC ZEM-3 instrument under 0.1 atm of He from room temperature to 873 K and back to room temperature. Measurements were performed twice to verify results. A Netzsch LFA 457 instrument was employed to measure thermal diffusivity using the laser flash method, between room temperature and 1123 K. Dense pellets were used for the measurements and a graphite spray was applied before measuring to minimize emissivity errors. As the electrical and thermal transport properties were measured at different temperature intervals, zT was calculated by interpolation of the thermal conductivity to the same temperatures as the electrical transport measurement.

The electronic structure of *hH* NbCoSn was calculated using density functional theory (DFT) as implemented in the Vienna *ab initio* Simulation Package (VASP)[34,35] with projector-augmented wave (PAW) pseudopotentials.[36,37] For structure optimization and band structure calculations, the Perdew-Burke-Ernzerhof (PBE) exchange-correlation functional within the generalized gradient approximation (GGA-PBE) was employed.[38] The standard primitive unit cell of the conventional face-centered orthorhombic cell was obtained using AFLOW.[39] A Γ center k-mesh of 8×8×8 was employed. Additional calculations of the density of states (DOS) employed the HSE06 screened hybrid functional.[40] Calculations of κ_{min} were conducted following Clarke[30] using the Young's modulus calculated from VASP using the Voigt-Reuss-Hill approximation.[41]

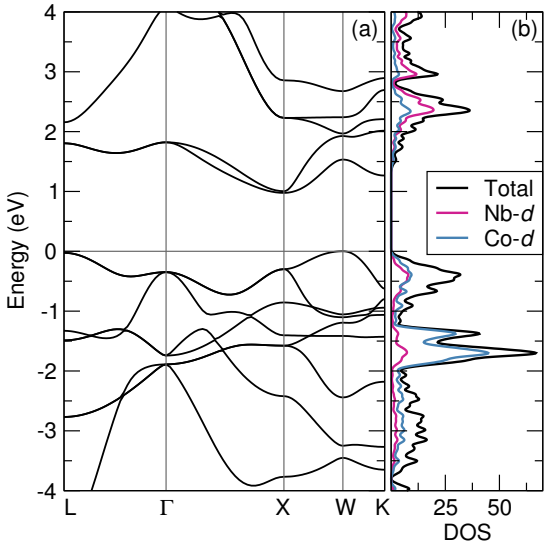

FIG. 2. (a) PBE electronic band structure displaying an indirect band gap in *hH* NbCoSn. (b) HSEO6 density of states for NbCoSn, showing a gap of almost 1.3 eV.

RESULTS AND DISCUSSION

Computational

The results of first-principles DFT calculations of the electronic structure of *hH* NbCoSn are displayed in Figure 3, including (a) the band structure, calculated using the PBE functional, and (b) the density of states, calculated using the hybrid HSE06 functional for greater reliability in establishing a band gap. NbCoSn is seen from DFT with GGA approximation to possess an indirect gap close to 1.3 eV. The band structure calculation suggests a band structure with a smaller band gap, closer to 1.0 eV. Given that this compound is n-type (from the Seebeck coefficient, discussed presently), it is relevant to consider the nature of the conduction band, which is largely comprised of Nb d states. The conduction band minimum at the X point is doubly degenerate and relatively flat. As the Seebeck coefficient is related to the effective mass, this result may explain the relatively high Seebeck coefficient.[1] These results are in contrast with the electronic structure of the more widely studied n-type thermoelectric *hH* TiNiSn, which has a valence band minimum that is singly degenerate at the X point. DFT calculations estimate a minimum lattice thermal conductivity, κ_{min} of 0.86 W m^{-1} K^{-1}. This value is lower than experimental measurements κ approaching 4 W m^{-1} K^{-1} at 1100 K.

Structural Characterization

In order to understand the thermoelectric properties of these compounds, it is first essential to evaluate them

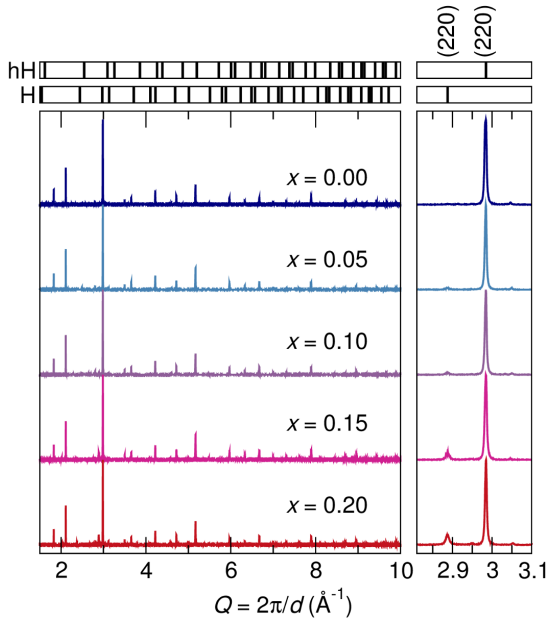

FIG. 3. Powder synchrotron X-ray diffraction results for the as-prepared (AP) $NbCo_{1+x}Sn$, $x = 0.00$ through 0.20 (indicated) samples. Indexed peaks from the refined lattice constants for the hH $F\bar{4}3m$ and H $Fm\bar{3}m$ phases are shown in the top two panels. (220) peaks are shown in detail on the panel to the right, where the evolution of the H phase can be observed with increasing x.

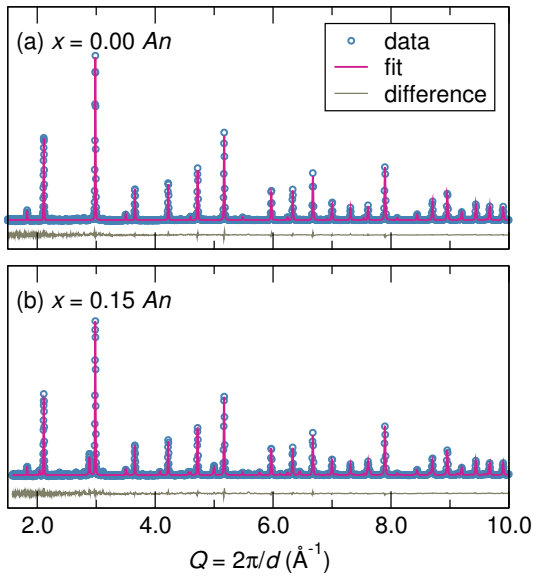

FIG. 4. Fits obtained from the Rietveld refinement of powder neutron diffraction data for the annealed (An) samples of $NbCo_{1+x}Sn$, with (a) $x = 0.00$, using a single hH phase, and (b) $x = 0.15$ refined with hH and H phases.

TABLE I. Structural parameters of the hH phase as obtained from Rietveld refinement of the neutron diffraction data, comparing AP and An samples. Note the greater degree of site-ordering in the An samples.

	$x = 0.00$, AP	$x = 0.00$, An	$x = 0.15$, An
a (Å)	5.95786(2)	5.95240(2)	5.95301(2)
Nb U_{iso}	0.0035(5)	0.00288(3)	0.0038(4)
Co U_{iso}	0.0030(2)	0.0031(2)	0.0025(2)
Sn U_{iso}	0.0029(4)	0.0032(4)	0.0018(3)
Occ. Nb_{Nb}	0.90(2)	0.97(2)	1
Occ. Co_{Co}	1	1	1
Occ. Sn_{Sn}	1	1	1
Occ. Co_{Nb}	0.10(2)	0.03(2)	0
R_{wp}	5.7%	6.2%	6.45%

from a structural perspective. This was accomplished through the analysis of the average structure of the Nb–Co–Sn series through synchrotron X-ray and neutron diffraction studies. Synchrotron X-ray diffraction provides the high Q-space resolution and high signal-to-noise necessary to consider the evolution of the minor H phase and determine impurity phases, while neutron diffraction allows for accurate determination of site occupancies and atomic displacement parameters (ADPs, reported as U_{iso}). Together, these techniques can provide a detailed description of the structural phases and atomic parameters of these hH–H materials, in particular the average structural disorder and its role on the observed physical properties.

Synchrotron X-ray diffraction was performed on $x = 0.00$, 0.05, 0.10, 0.15, 0.20 AP and $x = 0.00$, 0.15 An samples. The results for the AP samples are presented in Figure 3, and the evolution of the H (220) reflection, highlighted in the right panel, corresponds to increases in x-content. Rietveld refinement of the X-ray diffraction data indicated small weight fractions of secondary phases, including Nb_3Sn, elemental Sn, and an unidentified intermetallic phase. Secondary phases (Sn and Nb_3Sn) were less than 2wt%, and were thus not included in the overall fits of the diffraction data. The An samples have a smaller percentage of secondary phases, indicating the additional annealing step results in the dissolution of secondary phases remnant from the melting process. In addition to phase purity, there is a slight decrease in the lattice constant with additional annealing as is indicated by a comparison of the AP and An samples where $x = 0.00$ ($a = 5.9559(1)$ Å for the AP material as compared to $a = 5.9510(3)$ Å for the An). This lattice contraction suggests the An samples have increased ordering, as will be shown by neutron analysis.

Powder neutron diffraction was completed at room temperature for a subset of samples ($x = 0.00$ AP and $x = 0.00$, 0.15 An). Results for the An samples are shown with the Rietveld fits in Figure 4. Key crystallographic parameters are compared in Table I. The ADPs, presented as U_{iso}, of these compounds are similar at each of these sites, indicating that the individual atomic sites have similar degrees of structural disorder. While completing this analysis, attempts were made to introduce

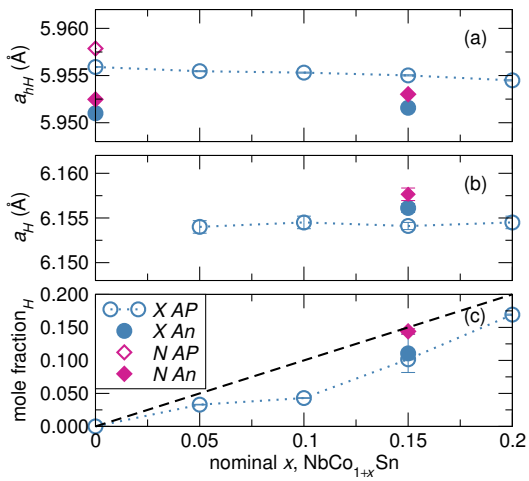

FIG. 5. (a) The lattice constant of the hH shows limited variation with x. Annealing is seen to yield samples with smaller lattice parameters, as a consequence of greater site ordering. (b) The H lattice constant is also not dependent upon x, but in contrast to hH, increases upon annealing. (c) The mole fraction of the H phase is close to the value expected from starting compositions. Results from powder synchrotron X-ray diffraction are denoted by X, and from powder neutron diffraction by N.

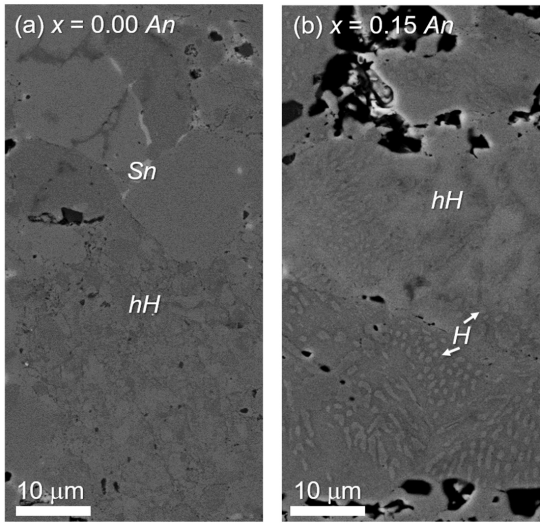

FIG. 6. SEM BSE results indicate the evolution of the H phase through increasing x, regions of H and hH phases are labeled alongside bright regions of Sn impurities. Micrograph (a) of $x = 0.00$ is almost entirely the hH phase while micrograph (b) of $x = 0.15$ shows the biphasic nature of the H phase through the addition of excess Co. The region shown in (b) was further evaluated by TEM, shown in Figure 7.

Co interstitials similar to the Ni interstials found in vacant tetrahedral sites of the TiNiSn system. However, these attempts resulted in the Co interstitial to have unreasonably large U_{iso} values, suggesting it to be an unfit model. While both of the $x = 0$ compounds have excess Co on the Nb 4a Wyckoff sites, this substitution is most evident in the AP sample as compared to the An samples. Additionally, occupancies of the annealed $x = 0.15$ compound indicates that the addition of the secondary H phase may encourage site ordering. Thus, the An samples have a higher degree of site ordering (*i.e.*, Co and Nb are occupying their predicted sites) in addition to having a higher phase purity.

Figure 5 compares the hH lattice constant, H lattice constant, and H mole fraction with respect to x. The synchrotron X-ray data indicates that the lattice constants of both phases are independent of composition in the range studied, indicating that the the addition of extra Co to the hH phase contributes to the formation of the H phase and not to the introduction of Co-interstitials in the hH phase. This result contrasts the lattice constant expansion found in the Ti–Ni–Sn system with the addition of Ni.[21] Furthermore, there is no evidence of peak splitting, as found in TiNiSn, that results from an extra phase with Ni interstials.[23] Figure 5(c) compares how the refined mole fraction of the H phase varies with nominal x. These results indicate that the H phase emerges near the 1:1 ratio with regards to the nominal compositions.

From these results, it is concluded that, regardless of annealing, as x is increased, the H phase will form as a second phase alongside the hH phase. Additionally, the extra annealing step in preparation of the An samples increases the site ordering of the hH phase as shown through a decrease in lattice constant and the degree of substitution of Co on the Nb sites. These results contrast the interstitial defects found in the TiNiSn system, exemplifying the variable forms of structural disorder that may appear within the Heusler family.

Microscopy

In addition to exploring the proportions of the phases and ordering in hH and H compounds, the microstructure of this biphasic compound has been studied to evaluate the interfaces between the two phases. Representative SEM micrographs are given in Figure 6, where it is apparent that the $x = 0.00$ An compound is entirely the hH phase, as shown in frame (a). Regions of Sn impurities can be identified by their bright appearance. Particles of H evolve with Co addition, as shown in frame (b) evaluating the $x = 0.15$ An sample. Dark regions of micrographs are pores that formed during sample preparation. These H inclusions become large in the $x = 0.20$ AP sample. Intermediate compositions ($x = 0.05$, 0.10) show similar H features as $x = 0.15$, but are less frequent. Comparison of An to AP samples indicates a reduction in impurity phases, such as Nb_3Sn and Sn upon the introduction of the annealing step.

The TEM image of lamella taken from the two-phase region indicated in Figure 6(c) is shown in Figure 7 and clearly reveals the presence of precipitates with sizes

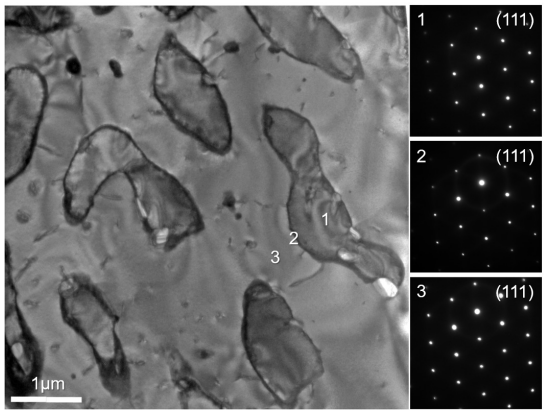

FIG. 7. TEM micrograph highlighting the interface formed between the H and hH phases in the annealed $x = 0.15$ sample. The section was taken from the lower right region of Figure 6(b). Selected area electron diffraction patterns are displayed at right for regions 1, 2, and 3 as indicated on the micrograph. These suggest the interface between the hH and H phases is semi-coherent.

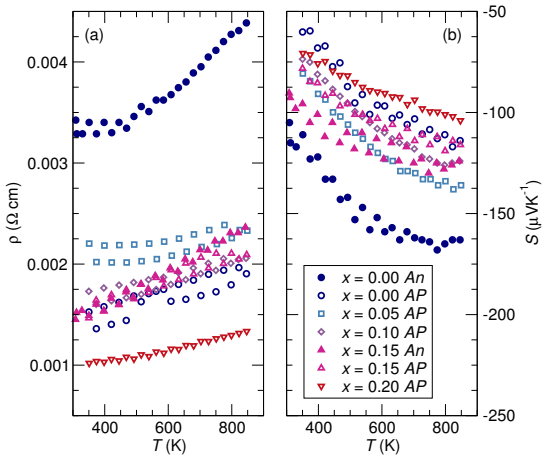

FIG. 8. (a) Electrical resistivity indicates that the $x = 0$ samples do not display the expected semiconducting behavior. An increase in metallic character is observed with increasing x while the (b) Seebeck coefficient generally decreases in magnitude with x. Annealing increases the resistivity of samples, suggesting the role of higher site ordering.

ranging from the nanometer to micron scale. A range of precipitate size will scatter phonons at a range of wavelengths, maximizing the reduction of κ.[25] The brighter particle is confirmed by EDX to be the H phase and the darker matrix as hH. The bright field TEM, Figure 7, is labeled to indicate the location for diffraction analysis. Selected area electron diffraction pattern (SAED) taken from the H phase, the hH phase, and the interface between the two indicates the same crystallographic orientation. This demonstrates a cube-on-cube orientation relationship between the H precipitates and the hH matrix with semi-coherent interfaces, which is expected due to their similar crystal structure and lattice parameter 3% misfit. Coherent interfaces are shown to significantly reduce the thermal conductivity without affecting the electrical conductivity, which is critical in designing a highly efficient thermoelectric material.[42]

Physical Properties

To determine the thermoelectric properties of the biphasic materials, a series of high temperature transport measurements were completed. The electrical resistivity (ρ), shown in panel (a) of Figure 8, indicates metallic behavior for all samples, as shown by the positive slope in the temperature dependence of the resistivity. This is in contrast to the semiconducting behavior of the hH compound as predicted through DFT. Since these calculations were performed on a perfectly ordered system, discrepancies can be attributed to the varying amounts of site ordering evidenced by the analysis of the diffraction data. A similar antisite disorder effect was proposed by Ono *et al.*,[27] who also predicted semiconducting behavior but observed metallic conductivity for samples of $NbCoSn_{1-x}Sb_x$. Additionally, we can observe that resistivity generally decreases with increasing x. In addition to compositional effects, an increase in the temperature dependence of the resistivity was observed for both An samples, in particular, the $x = 0.00$ An sample has a comparatively high electrical resistivity to the rest of the series. These observations can be attributed to the high degree of ordering present in the An sample, allowing it to be closer to its theoretical semiconducting state.

The Seebeck coefficient S is illustrated in panel (b) of Figure 8. The magnitude of the Seebeck coefficient decreases with increasing H content. The $x = 0.00$ An (no H phase) sample shows the largest magnitude in Seebeck coefficient, particularly when compared with the AP sample. This can be explained by the higher degree of ordering in the An sample as indicated by the structural characterization of these compositions.

The electrical resistivity is proportional to the magnitude of the Seebeck coefficient as both are dependent on carrier concentration.[1] This phenomenon is evident in this material system by observing that the sample with the lowest resistivity ($x = 0.20$ AP) is also the one with the lowest magnitude in Seebeck coefficient. Conversely, the sample with the highest resistivity ($x = 0.00$ An) has the largest magnitude in Seebeck coefficient. Therefore, as shown in Figure 9, varying x results in a limited change in the Power Factor, $S^2\rho^{-1}$.

Trends in the thermal conductivity, κ, as a function of temperature for $x = 0.00$, 0.15 (An, AP) are summarized in Figure 10.

The lattice contribution to thermal conductivity is shown for $x = 0.00$ An and $x = 0.15$ AP, as determined by subtracting the electronic contribution to thermal conductivity, as calculated by the Widemann-Franz law, from the experimental thermal conductivity.[43] A Lorenz

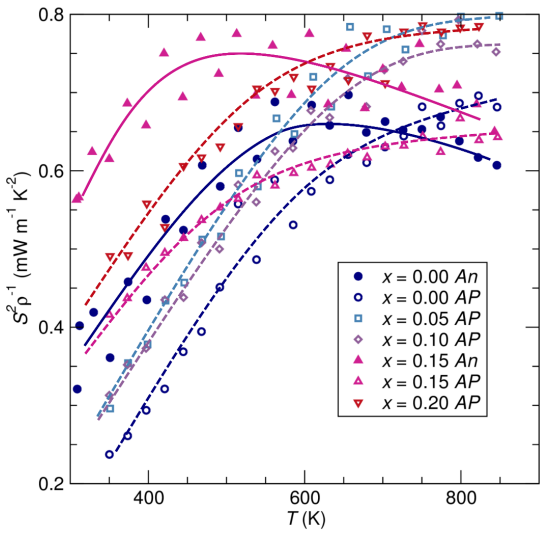

FIG. 9. The thermoelectric power factor, $S^2\rho^{-1}$ displayed for the different AP and An samples, as a function of temperature. At the highest temperature measured, there is a general trend towards a high power factor, suggesting that the decreased resistivity with increasing x, both for the AP and An, plays a greater role than changes in the Seebeck coefficient.

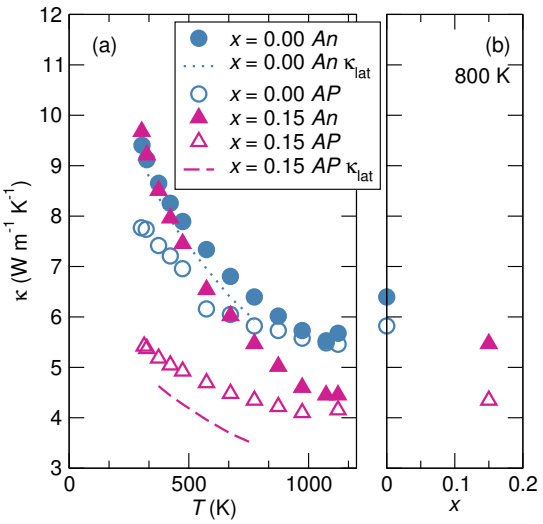

FIG. 10. Thermal conductivity (κ) for $x = 0.00$, 0.15 samples as (a) a function of temperature and (b) a function of x at 800 K. It is observed that both the absence of the additional annealing step and the inclusion of the secondary H phase reduces κ.

number of $2.44 \times 10^{-8} W\,\Omega\,K^{-2}$ was used. It can be observed that the addition of the H phase results in a decrease in κ over all temperature ranges. This is expected as the introduction of a secondary phase will disrupt the coherence of the material, resulting in less efficient phonon transport. Quantitatively, there is a 25% decrease in κ from $x = 0.00$ AP to $x = 0.15$ AP at 800 K. For both compositions, the AP samples have a lower κ than

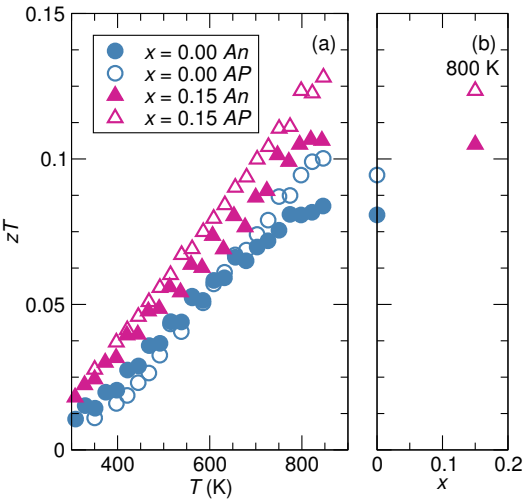

FIG. 11. Thermoelectric figure of merit, zT, of $x = 0.00$ and 0.15 as a function of (a) temperature and (b) x at 800 K. The largest zT was shown for $x = 0.15$ AP at 822 K, which is attributed primarily to the reduction in κ with the addition of a secondary H phase.

the An samples. This is attributed to both an increase in phase purity and site ordering induced by the annealing step, which decreases the amount of phonon scattering centers in the material. With κ reduction from both disorder and the secondary H phase, $x = 0.15$ AP exhibits the lowest κ. However, the κ of the AP samples approaches that of the An samples at higher temperatures, suggesting that with thermal cycling, performance of the AP will be closer to that of the An samples. Therefore, the most effective method for lowering κ is the inclusion of the secondary H phase.

The zT metric ($zT = [S^2/(\kappa\rho)]T$) for $x = 0.00$, 0.15 (An, AP) is shown in Figure 11. It is observed that zT reaches a maximum of 0.122 at 822 K for the $x = 0.15$ AP sample. As the power factors for all studied materials are similar at this temperature, the enhanced zT is attributed primarily to the reduction of κ. Comparing the maximum zT of the annealed, thermally stable, samples indicates 20% improvement in the thermoelectric figure of merit upon the introduction of $NbCo_2Sn$ inclusions. This confirms that the addition of a secondary phase is an effective method for optimizing the thermal aspects of the thermoelectric performance of these hH-H systems.

CONCLUSION

In summary, we have shown that hH compound NbCoSn will develop a biphasic structure with H $NbCo_2Sn$ through the introduction of excess Co. TEM shows the resulting interface is semi-coherent in nature. Two different preparation approaches, one which included a high temperature anneal, permitted the examination of antisite defects and their influence on trans-

port properties relevant to thermoelectric performance. In contrast to TiNiSn, results indicate that additional Co does not sit in the tetrahedral vacancies of the hH lattice, but may occupy Nb sites without a high temperature anneal. The annealed, highly ordered, compounds exhibit electrical resistivity closer to theoretical semiconductor behavior, while the experimentally examined compounds with antisite defects exhibit a reduction in thermal conductivity that, particularly in the biphasic compound, resulted in a thermal conductivity reduction and improvement in thermoelectric figure of merit, zT.

ACKNOWLEDGMENTS

This work was supported by the MRSEC Program of the National Science Foundation through DMR 1121053. M.L.C.B. is supported by the National Science Foundation Graduate Research Fellowship Program under Grant No. 1144085. The Materials Research Laboratory is a member of the NSF-supported Materials Research Facilities Network. Use of the Advanced Photon Source at Argonne National Laboratory was supported by the U. S. Department of Energy, Office of Science, Office of Basic Energy Sciences, under Contract No. DE–AC02–06CH11357. Neutron data was collected through the POWGEN mail-in service at ORNL's Spallation Neutron Source and was sponsored by the Scientific User Facilities Division, Office of Basic Energy Sciences, US Department of Energy.

[1] G. J. Snyder and E. S. Toberer, *Nature Mater.* **7**, 105 (2008).
[2] X. Yan, B. Poudel, Y. Ma, W. Liu, G. Joshi, H. Wang, Y. Lan, D. Wang, G. Chen, and Z. Ren, *Nano Lett.* **10**, 3373 (2010).
[3] J. Tang, H. Wang, D. Lee, M. Fardy, Z. Huo, T. Russell, and P. Yang, *Nano Lett.* **10**, 4279 (2010).
[4] M. Zebarjadi, G. Joshi, G. Zhu, B. Yu, A. Minnich, Y. Lan, X. Wang, M. Dresselhaus, Z. Ren, and G. Chen, *Nano Lett.* **11**, 2225 (2011).
[5] H. Kleinke, *Chem. Mater.* **22**, 604 (2010).
[6] X. Shi, J. Yang, J. Salvador, M. Chi, J. Cho, H. Wang, S. Bai, J. Yang, W. Zhang, and L. Chen, *J. Am. Chem. Soc.* **133**, 7837 (2011).
[7] J. He, and Y. Liu, *J. Mater. Res.* **26**, 1762 (2011).
[8] E. Toberer, A. May, and G. Snyder *Chem. Mater.* **22**, 624 (2009).
[9] T. Graf, C. Felser, S. Parkin, *Prog. Solid State Chem* **39**, 1 (2011).
[10] S. Chen and Z. Ren, *Matrl. Today* **16**, 387 (2013).
[11] F. Heusler, *Verhandl. Deut. Physik. Ges.* **5**, 219 (1903).
[12] S. Tsunegi, Y. Sakuraba, M. Oogane, K. Takanashi, and Y. Ando, *Appl. Phys. Lett.* **93**, 112506 (2008).
[13] S. Chadov, X. Qi, J. Kübler, G. Fecher, C. Felser, and S. Zhang, *Nature Mater.* **9**, 541 (2010).
[14] F. Tafti, T. Fujii, A. Juneau-Fecteau, S. Cotret, N. Doiron-Leyraud, A. Asamitsu, and L. Taillefer, *Phys. Rev. B* **87**, 184504 (2013).
[15] A. Planes, L. Mañosa, and M. Acet, *J. Phys.: Condens. Matter* **21**, 233201 (2009).
[16] S. ˙Ogut and K. M. Rabe, *Phys. Rev. B*, **51**, 10443 (1995).
[17] H. Kandpal, C. Felser, R. Seshadri, *J. Phys. D: Appl. Phys.* **39**, 776 (2006).
[18] S. Bhattacharya, A. Pope, R. Littleton, T. Tritt, V. Ponnambalam, Y. Xia, and S. Poon, *Appl. Phys. Lett.* **77**, 2476 (2000).
[19] Q. Shen, L. Chen, T. Goto, T. Hirai, J. Yang, G. Meisner, and C. Uher, *Appl. Phys. Lett.* **79**, 4165 (2001).
[20] W. Xie, A. Weidenkaff, X. Tang, Q. Zhang, J. Poon, T. Tritt, *Nanomatrl.* **2**, 379 (2012).
[21] J. E. Douglas, C. S. Birkel, N. Verma, V. M. Miller, M.-S. Miao, G. D. Stucky, T. M. Pollock, and R. Seshadri, *J. Appl. Phys.* **115**, 043720 (2014).
[22] J. E. Douglas, M. P. Echlin, W. C. Lenthe, R. Seshadri, and T. M. Pollock, *APL Mater.* **3**, 096107 (2015).
[23] J. E. Douglas, P. A. Chater, C. M. Brown, T. M. Pollock, and R. Seshadri, *J. Appl. Phys.* **116**, 163514 (2014).
[24] J. Makongo, D. Misra, J. Salvador, N. Takas, G. Wang, M. Shabetai, A. Pant, P. Paudel, C. Uher, K. Stokes, P. Poudeu, *J. Solid State Chem.* **184**, 2948 (2011).
[25] K. Biswas, J. He, I. Blum, C. Wu, T. Hogan, D. Seidman, V. Dravid, M. Kanatzidis *Nature* **489**, 414 (2012)
[26] Y. Kimura and Y. Chai *JOM* **67**, 233 (2014).
[27] Y. Ono, S. Inayama, H. Adachi, and T. Kajitani, *Jpn. J. Appl. Phys.* **45**, 8740 (2006).
[28] Y. Kimura, Y. Tamura, and T. Kita, *Appl. Phys. Lett.* **92**, 012105 (2008).
[29] Y. Kimura, Y. Tamura, and T. Kita, *Mater. Res. Soc. Symp. Proc.* **1044**, U07-06 (2008).
[30] D. Clarke, *Surf. Coat. Technol.* **163**, 67 (2003).
[31] A. C. Larson and R. B. Von Dreele *Los Alamos National Laboratory Report* **86-748** (2000).
[32] B. H. Toby, *J. Appl. Cryst.* **34**, 210 (2001).
[33] K. Momma and F. Izumi *J. Appl. Cryst.* **41**, 653 (2008).
[34] G. Kresse and J. Fürthmuller *Comput. Mater. Sci.* **6**, 15 (1996).
[35] G. Kresse, M. Marsman, J. Fürthmuller, and J. Vienna Ab-Initio Simulation Package: VASP the GUIDE. (2012).
[36] Blochl P. E. Blöchl, *Phys. Rev. B* **50**, 17953 (1994).
[37] G. Kresse and D. Joubert *Phys. Rev. B* **59**, 1758 (1999).
[38] J. Perdew, K. Burke, and M. Ernzerhof *Phys. Rev. B* **77**, 3865 (1996).
[39] S. Curtarolo, W. Setyawan, G. Hart, M. Jahnatek, R. Chepulskii, R. Taylor, S. Wang, J. Xue, K. Yang, O. Levy, M. Mehl, H. Stokes, D. Demchenko, and D. Morgan *Comput. Mater. Sci.* **58**, 218 (2012).
[40] J. Heyd, G. Scuseria, and M. Ernzerhof *J. Chem. Phys.* **118**, 8207 (2003).
[41] R. Hill *Proc. Phys. Soc. A* **65** 349 (1952).
[42] X. Huang, X. Wang, and B. Cook, *J. Phys. Chem. C* **114**, 21003 (2010).
[43] A. May, E. Toberer, A. Saramet, and G. Snyder, *Phys. Rev. B* **80**, 125205 (2009).